Spark Ablation Generation of Metal Nanoparticles and Coating on TiO₂ in the Aerosol Phase

Benjamin Gfeller, [a] Mariia Becker, [a] Nicolas Bukowiecki [a], Adrian Dario Aebi [a], Marcus Wyss [b] and Markus Kalberer [a]*

Generation and characterisation of metal nanoparticles (NP) gained attention in recent years due to their significant potential in applications as diverse as catalysis, electronics or energy storage. Despite the high interest in NPs, their characterization is challenging and detailed quantitative information on size, number concentration and morphologies are key to understand their properties. In this study we generated NPs from four metals, Au, Pt, Cu and Ni, via spark ablation in the aerosol phase, which allows to produce NPs as small as 1 nm in high quantities and purity. Particles were characterised with transmission electron microscopy (TEM), scanning transmission electron microscopy (STEM) and energy dispersive X-ray spectroscopy (EDX) as well as online aerosol particle size distribution measurement techniques. Particle modes for the four metals ranged between 3 nm and 4 nm right after generation. The number and size of particles generated correlated with thermal properties of the metals such as thermal or electrical conductivity. The four metal NPs were also coagulated with larger TiO₂ NPs of about 120 nm size and the metal surface coverage of the TiO₂ particles was characterised with electron microscopy and EDX spectroscopy.

Introduction

Nanoparticles (NPs) have long been discovered to be useful given their unique physical and chemical properties such as their changed hardness, elastic modulus, adhesion force[1,2] as well as electronic, optical and catalytic properties[3–6] compared to bulk material. Understanding the working principles on the nano-scale is crucial for new applications to emerge and for already applied uses in energy harvesting[7], medicine[8], electronics[9] etc. to be improved.

There is a wide range of generation methods for metal NPs ranging from chemical methods such as chemical reduction[10] and sol-gel methods[11] to physical methods like laser or spark ablation [12–14]. Chemical approaches are well established often yielding reproducible output within narrow particle size distributions usually produced in batch processes.[15–17] However, the purity of the generated particles can be compromised due to solvent residues or the toxicity of reagents can pose challenges.[16,17] In comparison, in physical generation methods, particles are often generated in an inert gas, allowing for a continuous particle production usually yielding particles in high purity due to the absence of liquid precursors and solvent.[18]

Spark discharge generation (SDG) is a precursor-free aerosol particle generation method that produces a high quantity and purity of NPs. During particle generation in SDG, electrode material is evaporated in the vicinity of an electrical spark initiated via the break-down of a high voltage difference applied to the electrodes.

The discharge occurs on time scales of microseconds and is accompanied by a temperature of around 20'000 Kelvin[19]. At these temperatures, the electrode material is evaporated and immediately mixed with a carrier gas where the electrode vapor expands rapidly and cools down with quenching rates of 10^7 Ks^{-1} resulting in the homogeneous nucleation of the evaporated electrode material to NPs with sizes well below 10 nm. [20] This method is highly versatile as every conductive pure element or alloy which is solid at working conditions can be used for particle generation. [14] Compared to laser ablation, no high energy lasers are needed for SDG particle generation, making it technically a more straight forward process. [21] The generation of metal NPs via SDG has gained increasing attention in recent years [22–24] due to the many potential applications of NPs e.g., in catalysis[25], nanoprinting[26] and drug delivery[8].

Quantification of NPs generated in the gas phase with diameters in the 1-5 nanometer range is challenging.[27] Given their high diffusion coefficients[28], sampling must occur rapidly after particle generation to minimise losses due to diffusion to walls of the experimental setup. Currently available techniques to determine aerosol NP number size distributions mainly use size classification via mobility analysis using differential mobility analysers (DMA) and detection via condensation particle counters (CPC) or electrometers.[29] Electrical mobility methods suffer from low charging efficiencies for particles in the low nm size range[30] resulting in low

a. Department of Environmental Sciences, University of Basel, 4056 Basel, Switzerland. E-mail: markus.kalberer@unibas.ch
b. Swiss Nanoscience Institute, University of Basel, 4056 Basel, Switzerland.

detection efficiencies. Although CPCs can detect particles to sizes down to about 2nm (31), detection is challenging because particles need to get activated in a supersaturated vapour (usually butanol or water) before detection of the activated particle by light scattering and because of diffusional losses of the smallest particles. Furthermore, these methods do not provide a way to assess particle morphologies. High-resolution imaging techniques are required for morphological analysis of particles as small as 1 nm and electron microscopy is an alternative method to determine particle number and size distributions down to 1nm or below.(32,33)

Manipulation of NPs generated in the gas phase include coating of the surface of larger (substrate) particles with small NPs resulting in particles with complex chemical or physical properties as well as targeted electric field assisted deposition on substrate layers for nanoprinting applications.(20,26,34). Metal NPs can be used as coating for semiconducting particles such as TiO_2, MgO or CuO_2.(35–38) Gas phase coatings are mediated by a fast mixing of two particle species and lead to high coating efficiencies. (20,24)

Different routes to assess coating efficiencies with NPs are available. Microscopic imaging can image coating structures and assess them qualitatively in high resolution.(20,34) For a quantification of the coatings, such techniques can also be used but usually only a small number of coated particles can be assessed due to the time consuming analysis.(34,39) Furthermore, measurements of the aerosol number size distributions of the individual composites and during the coating via mobility sizing and counting are often conducted to assess the coating. (39,40)

In this study we investigated the size distribution of four SDG-generated metal NPs (Au, Pt, Cu and Ni) and their coagulation

characteristics with larger TiO_2 particles. The mode of the size distributions for the four metal NPs is between 3 and 4 nm and increases with coagulation time due to coagulation. A detailed qualitative description of NP morphologies was conducted utilizing parameters such as primary particle size and the fractal dimension Df using high resolution transmission electron microscopy (TEM).

Furthermore, in bi-modal coagulation experiments of metal NPs with TiO_2 NPs, coating efficiencies and coating structure are assessed using numerous methods including gravimetry, TEM, scanning transmission electron microscopy (STEM) and STEM-electron dispersive X-ray spectroscopy (STEM-EDX) and compared with a numerical coagulation and diffusion model.(41,42)

Experimental

Figure 1 shows a general overview of the experimental setup to generate particles and collected them for characterisation.

Particle Generation and Mixing

Metal NPs were generated with a spark discharge generator (SDG) (VSParticle, Model G1, Delft, NL) (Figure 1, A). In a spark generator, the breakdown of a high voltage applied to two electrodes causes a discharge spark. The high temperatures of the spark (up to 20'000 K) evaporate electrode material, which is quickly quenched in a cooling gas flow causing the evaporated material to condense into particles consisting of the electrode material.

To ensure comparability, the break down voltage of the instrument was set to 1 kV with a current of 5 mA in all experiments. Au, Pt, Cu and Ni nanoparticles were generated
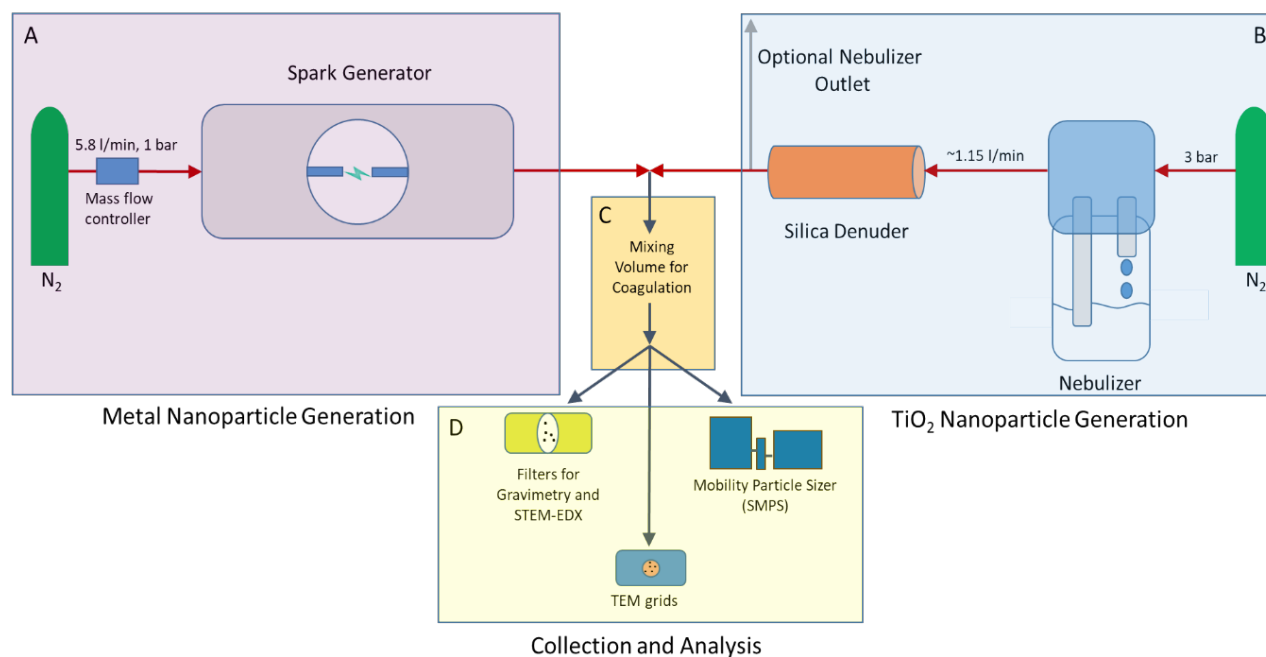

Figure 1 - Schematic of the setup used to generate (A, B), process (C) and analyze (D) the metal NPs. The spark generated particles (A) are either mixed with nebulized TiO_2 substrate NPs (B) in a variable volume for coagulation (C) or directly analyzed with transmission electron microscopy (TEM), scanning transmission electron microscopy (STEM) and STEM in combination with energy dispersive X-ray spectroscopy (STEM-EDX) and by scanning mobility particle sizing (SMPS) (D). Before collection and analysis, the aerosol is processed for mono-modal or bi-modal coagulation with coagulation times of 1.3 s, 2.2 s or 26.0 s. For analysis, the aerosol particles are collected on grids (for TEM, STEM and EDX) and on Teflon filters (for gravimetry) or analyzed directly in the gas phase with an SMPS.

with the SDG using electrodes of the respective metal with a purity of 99.99% and a diameter of 3 mm. The SDG was run in crossflow mode, where the quenching gas N_2 (99.999% purity) entered the spark chamber perpendicular to the electrodes at the position of the spark. If not specified otherwise, the N_2 flow rate was set to 5.8 l/min. To decrease instabilities in the particle generation, the system ran for 20 min before further particle processing and collection. This equilibration process was monitored using a scanning mobility particle sizer (SMPS, DMA model 3085, CPC model 3776, TSI, Shoreview, USA).

In addition to metal nanoparticles, TiO_2 aerosol particles were generated, using a home-built nebulizer (Figure 1, B) containing a 1%wt suspension of TiO_2 particles in the rutile and anatase phase (99.5% purity, Sigma Aldrich, Burlington, USA) with a BET determined particle size <100nm. The nebulizer inlet is pressurized with N_2 (99.999%) at a pressure of 3 bar. MiliQ® (resistance >18 MΩ) water was used for the preparation of the suspension to minimise impurities. Before use, the TiO_2 suspension was sonicated for 10 min and stirred continuously during operation to minimize coagulation within the suspension. The nebulized aerosol with a flowrate of 1.2 +/- 0.1 l/min passed through a cylinder filled with amorphous silica to reduce the relative humidity to < 2%. Analogously to the SDG, the nebulizer was left to equilibrate for 30 min before the analysis.

After exiting the SDG or the nebulizer, the aerosol particles entered a variable mixing volume (Figure 1, C) with coagulation times of 1.3 s, 2.2 s or 26.0 s, respectively, to allow for mono- or bi-modal coagulation (coating). If not mentioned otherwise, conductive Tygon tubing was used throughout the set up.

Particle Collection

Aerosol particles were collected on transmission electron microscopy (TEM) grids, filters or on TiO_2 substrate films. For TEM, scanning transmission electron microscopy (STEM) and STEM in combination with energy dispersive X-ray spectroscopy (STEM-EDX) particles were collected in a diffusional collection chamber on TEM grids (Quantifoil® R 1.2/1.3 on Cu or Au 200 mesh grids + 2 nm C, Grosslöbichau, Germany) for 2 h for each configuration unless mentioned otherwise. Teflon filters (2 μm pore size, 47 mm diameter, Pall Corporation, Port Washington, USA) were installed after the coagulation volumes to collect the aerosol particles for gravimetric analyses for 6h for all metals.

Alternatively, a film of TiO_2 substrate (TiO_2 electrodes opaque, Solaronix, Aubonne, CH) was installed in the pathway and exposed to a metal aerosol flow for 1h (Au), 6h (Au and Pt) and 12h (Cu, Ni).

Particle Analysis

Several measurement techniques were used to characterise metal and TiO_2 NPs (Figure 1, D). Particles were analysed with TEM as well as STEM and STEM-EDX (JEM-F200 cFEG, Jeol, Tokyo, Japan). For STEM, high-angle annular dark-field (HAADF) and annular bright-field (ABF) detectors were used. Au, Pt, Cu and Ni particles were measured separately or coated on TiO_2, in TEM mode. The coated aerosol particles were further analysed

in STEM mode and STEM-EDX. The image analysis tool ImageJ (Fiji, v.1.54.f) was employed for quantification and characterization of the particles. After differentiation of the particles and the background grid via manual adjustment of the colour threshold of the images, quantitative (2D projected area and number of particles) and qualitative information (morphology) were determined.

Gravimetric measurements of particles collected on Teflon filters were conducted using a high precision balance (Model XPR2, Mettler Toledo, Columbus, USA).

For STEM-EDX analysis of metal NPs coated TiO_2 films, lamellas (thin cross sections of the films) were prepared using a FEI Helios NanoLab 650 DualBeam (FEI, Hillsboro, USA). Depending on which metal NPs coating was deposited on the TiO_2, a protective layer of gold or carbon was deposited with a sputter coater or a carbon coater. Since the TiO_2 film surface is rough, a layer of about 100nm thickness was deposited. To prevent damage from ions an additional double layer of platinum or carbon is deposited. The first Pt or C-layer was deposited using electron-induced deposition at a beam energy of 5 keV and a beam current of 3.2 nA. The second Pt or C-layer was deposited with ion-induced deposition at a beam energy of 30 keV and a beam current of 83 pA. Sample cutting and polishing were carried out with the focused ion beam at a beam energy of 30 kV and beam currents ranging from 240 pA down to 83 pA. The sample thickness was < 75 nm. The imaging of TEM lamellas was carried out with a JEOL JEM-F200 instrument operated in STEM-mode at a beam energy of 200 kV.

A scanning mobility particle sizer (SMPS, TSI, Shoreview, USA) consisting of a soft X-ray neutralizer (Model 3087), electrostatic classifier (Model 3080), DMA (Model 3085), CPC (Model 3776) was used to monitor particle size distributions. The instrument was operated with a 1.5 l/min sample flow and a 15 l/min sheath air flow and a scanning range of 1.5 nm to 64 nm with a theoretical D50 of 2.5 nm of the CPC.

Finally, a numerical coagulation model based on Zhang et al. (42) was compared with measurement results to assess bi-modal coagulation of Au NPs on TiO_2 NPs. Details about the model can be found in the supplement.

Results and Discussion

Metal Nanoparticles

Particle Morphologies. Au, Pt, Cu and Ni metal NPs were generated with the SDG and collected for 2 hours, approximately 1.3 s after exiting the spark generator via diffusion on TEM grids and were analysed via TEM for their
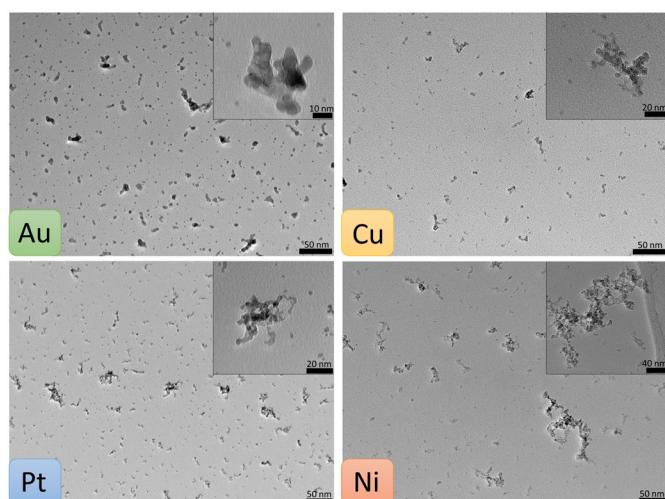
Figure 2 - TEM micrographs of spark generated Au, Cu, Pt and Ni NPs (a) - (d). The aerosol particles were collected via diffusion for 2h after 1.3 s. Morphologies range between mostly spherical (Au) to increasingly fractal-like (Pt, Cu, Ni) particles.

morphology. As depicted in Figure 2, which shows TEM micrographs of all four metals, particle sizes range between < 2 nm up to > 50 nm for all metals. Significant differences in number concentrations and morphologies are visible as summarized in Table 1.

The particles morphology was assessed by calculating their circularity using equation 1, where value between 0 and 1 are obtained and where a value of 1 corresponds to fully spherical particle and values going towards 0 to increasingly elongated shapes. Au particles are most spherical with an average circularity of about 0.8 (Table 1) whereas Cu and Ni have circularity values around 0.6.

$$Circularity = 4\,\pi \frac{Projected\ Particle\ Area}{Perimeter^2}\ \ (eq.\ 1)$$

Au formed fully spherical (i.e. coalesced) particles up to almost 6 nm whereas for Pt, Cu and Ni this threshold was at 2.5nm, 1.3nm and 1.1nm, respectively. Fully coalesced particles are defined here as primary particles. The maximal size for primary particle sizes was determined from particle circularities plotted against the surface equivalent diameter for each metal (Figure S1). The data was fitted with a logistic function and a relative

decrease of the fit of 10 % with increasing size was defined as the maximal primary particle diameter. 10% was chosen to ensure persisting sphericality. For larger particles, aggregates were observed abundantly, i.e. formation of a neck between two primary particles, but no full coalescence, and agglomerates, i.e. loosely combined particle assemblies.

Reasons that particle morphologies differ for the four metals are manifold. Particle growth is strongly material, size and temperature dependent. Initial coalescence occurs within the spark generator under rapid cooling of the supersaturated vapor. However, coalescence and aggregation can continue well below the bulk melting points of the individual metals (43). Significantly lower melting points for particles in the low-nm size range compared to bulk values have been estimated (see Table 1) because of the increased surface to volume ratio associated with large internal stress.(44,45) As we generate particles as

small as 1 nm this melting point depression likely has a notable effect on the particle morphologies observed here, i.e. a more pronounced coalescence and a relatively later onset of agglomeration. Temperatures in Table 2 were obtained from sources using a thermodynamic liquid nucleation and growth model or molecular dynamics simulations. According to these models, Au particles of 2 nm size experience the lowest melting points (600 K; Table 1), which could explain the large diameter of primary Au particles of up to about 5.6 nm, whereas Pt exhibits the highest melting points, which might explain the lower primary particle size observed here. It is further reported that for Au particles liquid-like behaviour, i.e., having a high mobility surface layer, occurs down to room temperature. (46,47) Multiple studies describe Au particles smaller than approximately 3 nm as being liquid like at room temperature.(20,45)

For Cu and Ni particles a substantial melting point depression is estimated as well, but their primary particles are smaller than for Au and Pt. These elements are more prone to surface oxidation than Au and Pt (48,49), which results in higher melting points than estimated for the pure metals, preventing further coalescence/aggregation. (50,51) Given a metal electrode purity of 99.99% and a N2 carrier gas impurities of < 2 ppm, oxide layers are likely to form. (22)

Table 1 Parameters to quantify particle morphologies for particles collected after 1.3 s coagulation time and data on melting point depletion of NPs. (A) (52) (B) (53) (C) (54) (D) (55)

Metal	Average Circularity	Max. diameter of spherical *(primary)* particle [nm]	Fractal Dimension Df	Melting point for NPs (particle size 2 nm and 10 nm) and bulk [K] (references)
Au	0.79	5.6+/-0.3	1.75 +/- 0.05	600, 1200, 1338 (A)
Pt	0.71	3.2+/-0.1	1.76 +/- 0.05	1287, 1685, 2043 (B)
Cu	0.62	1.3+/-0.4	1.74 +/- 0.06	964, 1289, 1357 (C)
Ni	0.57	1.1+/-0.1	1.67 +/- 0.07	893, 1623, 1726 (D)

Further particle growth via agglomeration can be described quantitatively via the fractal dimension Df (Table 1) (56,57). Df values assessed via the determination of the radius of gyration for the four metals between 1.67+/-0.07 and 1.76+/-0.05 were determined from TEM micrographs and are in good agreement with the literature value for diffusion limited cluster-cluster aggregation of 1.77+/-0.03.(56)

This matches to the findings of a previous study (57) stating that spark generated aerosol particles are formed via diffusion limited cluster-cluster aggregation.

Particle losses within the spark generator. Particle losses inside the spark generator were estimated for all four metals by comparing the mass of metal NPs collected on a filter for 6 hrs immediately after the SDG with the mass that was ablated from both electrodes during the collection (Table 2). The electrode mass loss is lowest for Cu with 17 µmol and goes up to 82.5 µmol for Ni. The filter mass ranges between 5 µmol (Au and Cu) and 37 µmol (Ni).

The metal mass loss between generation and NP mass exiting the SDG (ratio between filter weight and electrode mass loss) is substantial and ranges between 54% (Ni) up to 91% (Au). The majority of the losses can be attributed to losses immediately after NP generation due to the high electric and magnetic fields present in the plasma of the spark which affects the charged particles.(21,58)

Reasons for the inter-metal differences in the total amount of ablated material strongly depends on its thermal properties. Lower thermal conductivities lead to a less effective cooling of the electrode material and hence more evaporation. (21,59) Furthermore, lower boiling points also lead to more evaporation. Hence, the highest ablated electrode mass of Ni could be explained by the low thermal conductivity combined with a low boiling point whereas in contrast, the lowest ablate electrode mass is found for Cu, which has the highest thermal conductivity (Table 3). The large ablated mass of Ni explains the large number of agglomerates >20 nm seen in Figure 2 and 3.

The higher relative losses of Au in the SDG can be explained by an increased Joule heating due to a lower electric conductivity combined with a relatively low melting point (Table 2). Due to the local heating of the electrodes, the formation of molten microscopic pools on the electrode surface can lead to the formation of large micron sized particles. (21) Ultimately, this might lead to losses of these large particle due to impaction within the spark chamber.

Furthermore, oxidation of the aerosol particles during generation as well as on the filter leads to an increase in total particle mass on the filter. This effect is most pronounced for the non-noble metals (i.e. Cu and Ni) but also occurs for Au and Pt. Thus, the mass losses within the spark generator are likely underestimated.

Aerosol particle size distributions. Figure 3 shows particle size distributions determined from TEM micrographs for all four metals with modes ranging from 2 nm (Pt and Cu) to about 3 - 4 nm (Au and Ni) for the shortest coagulation time of 1.3 s and increasing modes for the two longer coagulation times. Particle sizes are lognormally distributed as is expected given the sampling form a single-source aerosol(28)(Hinds, 1999). Total number concentrations for the shortest coagulation time are largest for Au and Pt and more than 60% lower for Cu and Ni. For the longer coagulation times (2.2 s and 26.0 s) fewer particle numbers are observed due to increased coagulation (resulting in to a shift of the mode to larger diameters) and diffusional losses to the tube walls. For Ni and Cu size distributions for the longer coagulation times could not be determined due to the overall smaller particle concentrations resulting in poor counting statistics.

Difficulties in particle detection in TEM for Cu and Ni also arise due to the lower resolution of the NPs during imaging for these two elements, which depends, e.g., on the atomic number ($\propto Z^2$) and the thickness of particles. Thus, given the lower atomic numbers of Cu and Ni (Z 29 and 28, respectively) and the smaller primary particles, Cu and Ni particles suffer from a lower resolution compared to Au and Pt (Z 79 and 78, respectively) particles. Although enhanced contrast can be achieved via image manipulation in ImageJ, the detection of particles with a diameter of a few nm is still challenging. The shaded bins in the case of Ni indicate the overestimation of the smallest particles due to the lower signal to noise ratio during particle detection with ImageJ.

Table 2 Amount of ablated material per metal combined with data on boiling points and thermal and electrical conductivity obtained from (59). Mean and standard deviation of triplicate measurements are given.

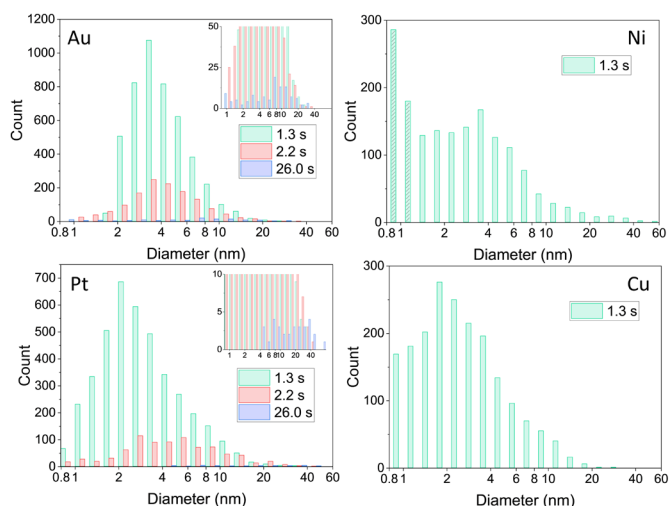| Metal	Mass loss electrode [µmol]	NP mass on filter [µmol]	Loss in Spark Generator [%]	Thermal conductivity [W m^{-1} K^{-1}]	Electric conductivity [10^{-8} Ω m]	Bulk Boiling point [K]	Bulk Melting point [K]
Au	54.5+/-9	5+/-0.5	91+/-1	318	2.03	3073	1338
Pt	46.5+/-2	9+/-1.5	80+/-2	72	9.82	4098	2043
Ni	82.5+/-8	37.5+/-2.5	54+/-4	93	6.24	3073	1357
Cu	17+/-6.5	5+/-0.5	66+/-19	402	1.73	2848	1726

Figure 3 - Metal NP number size distributions determined from TEM micrographs with ImageJ for three coagulation times for Au and Pt and 1.3 s coagulation time for Ni and Cu. After a coagulation time of 1.3 s, particle modes range from 2 nm (Pt and Cu) to approximately 3 nm for Au and Ni. Particle concentrations are significantly higher (> 300%) for Au and Pt compared to Cu and Ni. The shaded bins for Ni indicate an overestimation of the smallest particles due to a lower signal to noise ratio at these small particle sizes. Inserts for Au and Pt show the strongly decreased size distributions after a particle coagulation time of 26.0 s.
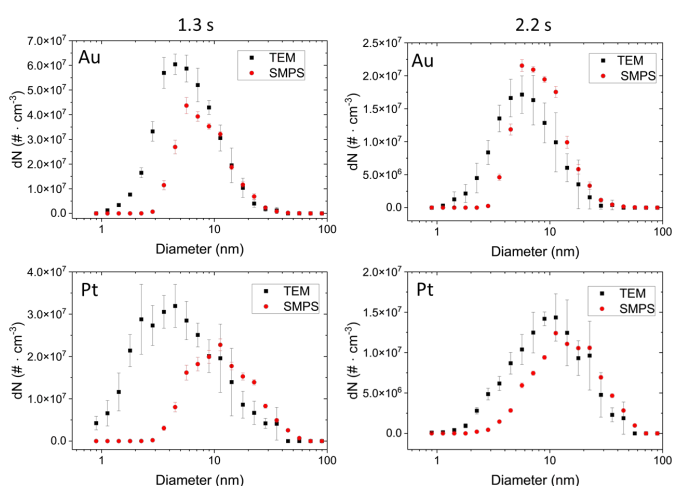

Figure 4 - Aerosol number size distributions estimated from TEM micrographs of Au and Pt NPs. The NPs were collected via diffusion for 2h for coagulation times of 1.3 s and 2.2 s and subsequently used to calculate the aerosol distributions (in black). In red, as a comparison, simultaneously measured SMPS distributions are plotted. Errors for the calculation consist of the propagate statistical error from triplicate measurements paired with multiple systematic errors. SMPS error bars consist of the standard deviation of the scans taken for an 1h average.

Particles are deposited on TEM grids due to diffusion in a laminar flow regime, which results in an overestimation of the smaller particles compared to the larger particles and therefore the size distribution displayed in Figure 3 is skewed towards smaller particle sizes compared to the size distribution present in the aerosol phase. This collection artefact can be corrected assuming that Brownian diffusion was the dominant particle collection process on the TEM grids. The dimension of the collection chamber, the diffusion coefficient of the particles and the flowrate of the aerosol stream **(28)** were used to calculate the particles number size distributions in the aerosol flow after a coagulation time of 1.3 s and 2.2 s, respectively, for Au and Pt (Figure 4, black data). Modes of the calculated size distributions in Figure 4 are shifted by approximately 1-2 nm to larger sizes compared to the histograms in Figure 3 as expected.

Figure 4 also displays the aerosol particle size distribution with measured with an SMPS (red data). For particle sizes > 10 nm the concentrations calculated from TEM analysis and measured by SMPS align well for all four examples shown in Figure 4. For particles smaller than 10 nm differences of the two size distributions become more pronounced the smaller the particle diameters are, due to the limited counting efficiency of the SMPS (DMA Model 3085, CPC Model 3776, TSI) at particle diameters below 5nm, leading to an underestimation of particles in this size range. Using the TEM derived size distribution of Au and Pt and a coagulation time of 1.3 s, nearly 50% and 60%, respectively, of all particles have a diameter < 5 nm. A comparison of coagulation time of 1.3 s and 2.2 s shows the growth of the mode of the size distribution for Au and Pt particles as is expected for longer coagulation times due to Brownian diffusion and hence, for a coagulation time of 2.2 s the SMPS distribution aligns more closely with the calculated TEM distribution (Figure 4).

Although TEM-derived particle sizes and SMPS measurements agree well for >10 nm particles, larger particles are affected by sampling uncertainties and thus lager errors in Figure 4: Due to the smaller number concentrations of particles >10 nm counting uncertainties increase for these sizes. Where several hundred or thousands of <10 nm particles diffuse onto the grid within the sampling time of 2h, larger particles are only collected at significantly lower numbers on the grid Figure 3). Moreover, smaller particles can more easily be assumed to be spherical whereas particles >10nm are mostly agglomerates. This results in an underestimation of the larger particles due lower diffusion constants of non-spherical particles compared to spherical ones.(60,61) Furthermore, uncertainties in particle size arise as an accurate size characterization is increasingly difficult for larger fractal-like particles when circular shapes are assumed in the size determination.

For Ni and Cu, challenges in particle detection with ImageJ (see discussion above) prohibited a detailed analysis. However, the results of the analysis for coagulation time 1.3 s can be found in Figure S2 in the supplement.

Metal Nanoparticle coating on TiO$_2$ Nanoparticles

Morphology of coating metal NPs. All four metal NPs, generated as described above, were mixed and coagulated with nebulized TiO$_2$ substrate particles (mode 120 nm, concentration about $8*10^6$ particles cm^{-3}) for 26 s and analysed with TEM, STEM and EDX. TEM micrographs (Figure 5) show significant differences in the coating with Au, Pt and Ni metal particles. Au and Pt exhibit a high density of 'island-like' coating, i.e. the presence of individual metal NPs on the TiO$_2$ surface, which are visible clearly at the edges of the TiO$_2$ substrate particle. Further towards the centre of the TiO$_2$ particles, the metal NPs are less visible due to the thick layer of TiO$_2$ particle which leads to a decrease in contrast for the metal particles.
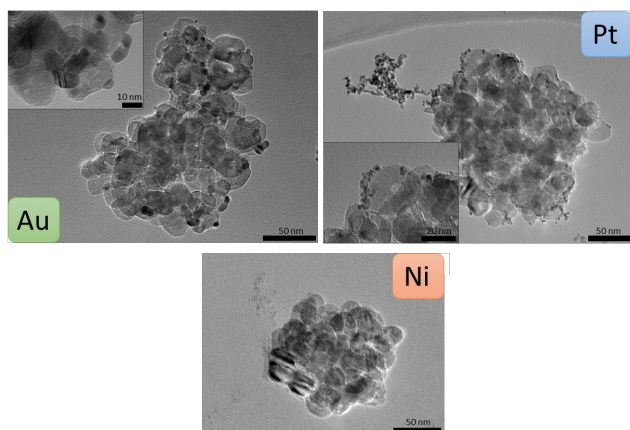
Figure 5 - TEM micrographs of TiO$_2$ substrate particles coated with Au, Pt, Cu or Ni NPs. For Au and Pt, the coating corresponds to the darker shapes predominantly visible at the edges of the substrate. Ni coating appears to be brighter than the substrate and is only visible on the right edge of the substrate particle.

For Au, the coating consists predominantly of primary particles and for Pt, a mix between primary particles and agglomerates with sizes up to well above 50 nm is observed. For Ni and Cu, no clear qualitative assessment of the coating was possible because these two metals produce significantly smaller primary particles in the spark generator (Table 1) and exhibit lower contrasts in TEM. While for Ni fractal-like particles are faintly visible at the edge of the TiO$_2$ substrate particle, no coating was detectable for Cu. The coating behaviour depends on various factors such as the thermodynamic properties of the particle species and the size and number concentration of the coating particles. Surface wetting, i.e. the inclination angle of a liquid, or liquid-like particle to spread and adhere to a substrate (TiO$_2$) particle, is a key concept to describe the coating. **(62)** Wetting depends on the particle size and the surface free energies of the involved species, i.e. metals and TiO$_2$ in our study. Metals

particles of a few nm in size can be considered liquid or liquid-like if the metal has a lower or equal surface free energy than the substrate species and thus surface wetting, i.e. smooth coatings can be expected. **(20)** Values for the surface free energies vary strongly in literature and depend on the techniques used to determine them, the crystal structures and the temperature and pressure of the measurement. TiO$_2$ has a surface free energy ranging between 0.6 and 1.3 Jm^{-2}.**(63)** Values for Au, Pt, Cu and Ni range between 1.4 Jm^{-2} and 1.9 Jm^{-2}.**(64,65)** Both, Au and Pt primary particles experience a slight wetting on the TiO$_2$ surface as can be seen in the inlays of Figure 5. A contact angle (Young angle) of 57 degrees for Au and of 63 degree for Pt was measured, i.e. well below 90 degrees, which was expected given that TiO$_2$ has a slightly lower surface free energy than the metal NPs and therefore partial wetting rather than a smooth coverage is expected. Ni and Cu likely exhibit the same behaviour due to the similar surface free energies but could not be confirmed as described above.

Size and concentration of coating metal NPs. In addition, STEM micrographs and EDX spectra were recorded for all metals on TiO$_2$ to assess the size distributions of the metal NPs that coagulated with TiO$_2$. EDX creates spectral maps which show the spatial distribution of the elements present in the sample and thus allows to distinguish between TiO$_2$ substrate and metal coating also in the centre of a TiO$_2$ particle. The EDX signal was integrated over 1h in order to achieve the highest possible resolution without disintegrating the particle due to exposure to the high energy electron beam. Figure 6 depicts the EDX recordings of the coating (green) for Au, Pt and Ni on TiO$_2$ particles (blue).
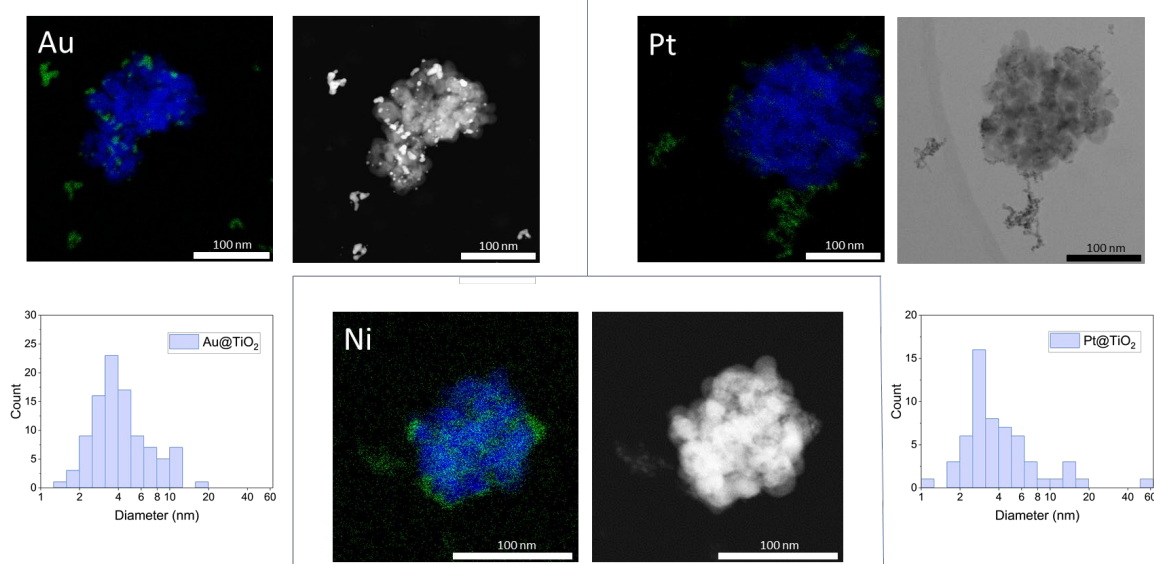

Figure 6 - STEM micrographs and STEM-EDX spectral mappings of TiO$_2$ substrate particles coated with Au, Pt or Ni. STEM was recorded using a HAADF detector in the case of Au and Ni, and an ABF detector in the case of Pt. The TiO$_2$ signal is colored blue and the coatings are in green for all metals. For Au and Pt, additional histograms of the number size distributions of the coating particles (i.e. 'metal@TiO$_2$') are displayed.
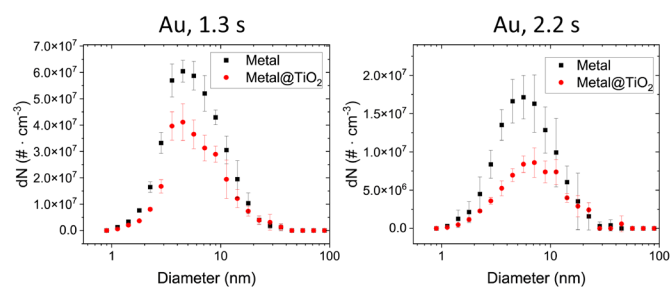
Figure 7 - Aerosol number size distributions estimated from TEM micrographs of uncoated Au NPs for mono-modal or bi-modal coagulation with TiO_2 NPs. For both coagulation times of 1.3 s and 2.2 s, the metal distributions during the coating (red, 'metal@TiO_2') were significantly lower than for the metal alone (black). This decrease is directly related to the TiO_2 particle coating. Error bars are shown for the propagated statistical error from triplicate measurements paired with multiple systematic errors.

Figure 8 - EDX spectral mappings of the cross-section of TiO_2 substrate films (in blue) coated with Au, Pt or Ni NPs (in green). The TiO_2 films were exposed 6h (Au and Pt) or 12h (Ni) to a metal NP flow. Individual particles are visible on the substrate for Au, Pt and Ni.

In the EDX mappings, coating particles and their elemental composition can be distinguished clearly from the substrate. In STEM micrographs (Figure 6) the spatial distribution of metal NPs on TiO_2 particles is also clearly visible, particularly for Au and Pt due to the dependence of the resolution of STEM analysis on the atomic number of the analysed elements.

Au and Pt coating particles are lognormally distributed on the substrate with a mode of approximately 3.5 nm for both metals (see histograms in Figure 6). This is slightly lower than the mode of the aerosol particle distributions of around 5 nm (Au) and 4 nm (Pt) determined in Figure 4. These discrepancies can be explained by the particle size dependence of the Brownian coagulation where the large TiO_2 particles scavenge smaller metal particles with a higher efficiency than larger metal particles.

The Ni NPs coating on TiO_2 could only be characterised qualitatively with EDX. Figure 6 shows >10 nm Ni agglomerates adsorbed to the TiO_2 surface, similar to the coating of Pt. Ni particles <10 nm are likely also present, but visualization proved to be challenging given the smaller size of the primary particles compared to Au and Pt (Table 1).

The particle size and number distribution of metal NPs coated on TiO_2 was also assessed from TEM analysis using the same approach as discussed for Figure 4. The Au NP aerosol particle size distribution was calculated from TEM analyses by counting the number and size of Au NPs on the TEM grids that did not coagulate with TiO_2 particles when Au and TiO_2 were mixed for 1.3 s and 2.2 s. This was compared to the size distributions when no TiO2 particles were present in the set up (as shown in Figure 4). The number concentration during coating (red datapoints in the Figure 7) is significantly lower than in the case when no TiO_2 particles are present (black datapoints, Figure 7) and a reduction of nearly 50% was determined of individual Au NPs ($4*10^8$ particle cm^{-3} to $2.56*10^8$ particle cm^{-3} for 1.3 s coagulation time), which were not attached to a TiO_2 particle on the TEM grid. This reduced concentration of individual Au NPs can be attributed to their coagulation (i.e. coating) with TiO_2 and serves as a lower boundary for the coating efficiency of > 1E8 per cm^3, i.e. 20 Au particles per TiO_2 substrate assuming $8*10^6$ TiO_2 particles cm^{-3}.

This is a lower estimate of the coating, because in the absence of TiO_2 particles (black data, Figure 7) Au-Au NP coagulation is more effective, lower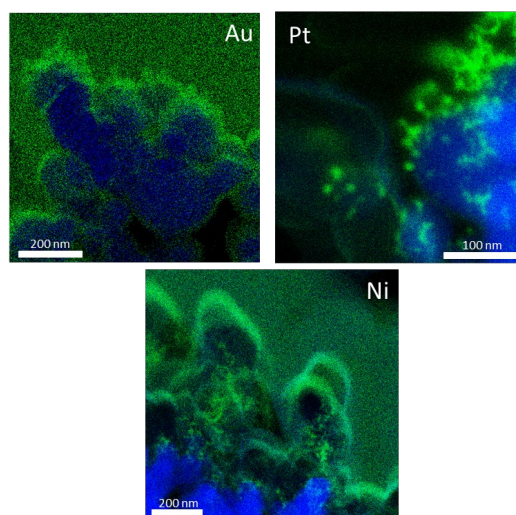ing the total particle concentration compared to the conditions when TiO_2 particles are present where Au NPs coagulation with TiO_2 is a competing process to the Au-Au coagulation. Therefore, higher number concentrations of primary Au NPs are coagulating with TiO_2 than estimated from the difference of the two number size distributions shown in Figure 7. This underestimation of Au NPs coagulating with TiO_2 is confirmed qualitatively by the larger number of Au NPs counted on TiO_2 particles with STEM/EDX analysis (Figure 6, histograms), where about 80-100 Au NPs per TiO_2 particle were counted.

To explore if a denser coating of metal NPs on TiO_2 particles could be achieved we deposited NPs on TiO_2 films via diffusion. The films were exposed for 6h (Au and Pt) or 12h (Ni) to a metal NP flow. Lamellas, thin cross sections of metal coated TiO_2 films, were then cut. The longer collection time for Ni is needed to improve the signal intensity in EDX due to smaller primary particles and lower aerosol particle concentration of Ni compared to Au and Pt. Cross-sections of the coated TiO_2 substrate layers were measured with STEM and EDX as depicted in Figure 8. For Pt and Ni individual particles are visible (i.e. island-like coating, green in Figure 8) which is in agreement with the observation of individual TiO_2 coating particles shown in Figures 5 and 6. Au particles appear to aggregate the most, and thus a continuous layer forms on the TiO_2 surface (blue in Figure 8) when exposed for 6h. As also seen in the previous section, Pt and Ni show similar coating behaviours for >10 nm particles. In contrast to Au, Pt and Ni both exhibit strong agglomerate formation with particles up to several hundreds of nanometres in size and even at long exposure times of 6h (Pt) or 12h (Ni), no continuous metal layer formation occurs on the TiO_2 particles.

The smooth green coating on the EDX mapping of Ni in Figure 8 is due to the Au sputtering layer on the TiO_2 film (see experimental section) and not due to Ni coating. Ni NPs are visible as faint green fractal structures in the lower half of the Figure, loosely attached to the blue TiO_2. In addition to the EDX recordings presented here, STEM micrographs can be found in the supplement.

Conclusions

In this study, we investigated spark generated metal NPs and their coating behaviour on TiO_2 substrate NPs in the aerosol phase. NPs of four different metals (Au, Pt, Cu, Ni) were characterized for size and morphology. Using TEM measurements, aerosol particle number size distributions of particles as small as 1 nm with modes of the size distribution of 3 – 4 nm were determined, which poses a significant challenge for commonly used aerosol particle size measurement techniques. Differences in particle size and number distributions for the four metals could be correlated with thermal properties of the respective metals, such as electrical and thermal conductivity and melting and boiling point.

Coating of the four metal NPs on TiO_2 substrate NPs via coagulation was characterised with TEM, STEM and EDX and showed that for all four metals individual coating particles partially wetted the TiO_2 substrate. Up to about 100 Au NPs were counted per TiO_2 particle. For Au, a continuous coating layer could be achieved by increasing the deposition time to several hours. A detailed characterisation of metal NPs and their coagulation and coating behaviour in TiO_2 particles could be important to evaluate and rationalise the catalytic behaviour of these particles in future studies.

Author contributions

Conceptualization – Mariia Becker and Benjamin Gfeller; investigation – Benjamin Gfeller, Mariia Becker and Adrian Dario Aebi; methodology (adaptation and model implementation) – Nicolas Bukowiecki and Benjamin Gfeller; methodology (image analysis) – Benjamin Gfeller; methodology (electron microscopy) – Marcus Wyss; project administration – Mariia Becker, Benjamin Gfeller; funding acquisition and supervision – Markus Kalberer; writing (original draft) – Benjamin Gfeller; writing (review and editing) – all authors.

Conflicts of interest

There are no conflicts to declare.

Data availability

Data are available from the corresponding author upon reasonable request.

Acknowledgements

References

1. Guo D, Xie G, Luo J. Mechanical properties of nanoparticles: basics and applications. J Phys D: Appl Phys. 2013 Dec;47(1):013001.

2. Khan I, Saeed K, Khan I. Nanoparticles: Properties, applications and toxicities. Arabian Journal of Chemistry. 2019 Nov 1;12(7):908–31.

3. Baig N, Kammakakam I, Falath W. Nanomaterials: a review of synthesis methods, properties, recent progress, and challenges. Mater Adv. 2021 Mar 29;2(6):1821–71.

4. Cuenya BR. Synthesis and catalytic properties of metal nanoparticles: Size, shape, support, composition, and oxidation state effects. Thin Solid Films. 2010 Apr 2;518(12):3127–50.

5. Jennings T, Strouse G. Past, Present, and Future of Gold Nanoparticles. In: Chan WCW, editor. Bio-Applications of Nanoparticles [Internet]. New York, NY: Springer; 2007 [cited 2024 Oct 23]. p. 34–47. Available from: https://doi.org/10.1007/978-0-387-76713-0_3

6. Terna AD, Elemike EE, Mbonu JI, Osafile OE, Ezeani RO. The future of semiconductors nanoparticles: Synthesis, properties and applications. Materials Science and Engineering: B. 2021 Oct 1;272:115363.

7. Ulmer U, Dingle T, Duchesne PN, Morris RH, Tavasoli A, Wood T, et al. Fundamentals and applications of photocatalytic CO2 methanation. Nat Commun. 2019 Jul 18;10(1):3169.

8. Murthy SK. Nanoparticles in modern medicine: State of the art and future challenges. International Journal of Nanomedicine. 2007 Dec 1;2(2):129–41.

9. He Z, Zhang Z, Bi S. Nanoparticles for organic electronics applications. Mater Res Express. 2020 Jan;7(1):012004.

10. Gudikandula K, Charya Maringanti S. Synthesis of silver nanoparticles by chemical and biological methods and their antimicrobial properties. Journal of Experimental Nanoscience. 2016 Jun 12;11(9):714–21.

11. Lu CH, Jagannathan R. Cerium-ion-doped yttrium aluminum garnet nanophosphors prepared through sol-gel pyrolysis for luminescent lighting. Applied Physics Letters. 2002 May 13;80(19):3608–10.

12. Ullmann M, Friedlander SK, Schmidt-Ott A. Nanoparticle Formation by Laser Ablation. Journal of Nanoparticle Research. 2002 Dec 1;4:499–509.

13. Nagarajan R. Nanoparticles: Building Blocks for Nanotechnology. In: Nanoparticles: Synthesis, Stabilization, Passivation, and Functionalization [Internet]. American Chemical Society; 2008 [cited 2024 May 13]. p. 2–14. (ACS Symposium Series; vol. 996). Available from: https://doi.org/10.1021/bk-2008-0996.ch001

14. Schwyn S, Garwin E, Schmidt-Ott A. Aerosol generation by spark discharge. Journal of Aerosol Science. 1988 Oct 1;19(5):639–42.

15. Daruich De Souza C, Ribeiro Nogueira B, Rostelato MECM. Review of the methodologies used in the synthesis gold nanoparticles by chemical reduction. Journal of Alloys and Compounds. 2019 Aug 25;798:714–40.

16. Jamkhande PG, Ghule NW, Bamer AH, Kalaskar MG. Metal nanoparticles synthesis: An overview on methods of preparation, advantages and disadvantages, and applications. Journal of Drug Delivery Science and Technology. 2019 Oct;53:101174.

17. Zhang Q li, Yang Z mao, Ding B jun, Lan X zhe, Guo Y juan. Preparation of copper nanoparticles by chemical reduction method using potassium borohydride. Transactions of Nonferrous Metals Society of China. 2010 May 1;20:s240–4.

18. Kumari S, Raturi S, Kulshrestha S, Chauhan K, Dhingra S, András K, et al. A comprehensive review on various techniques used for synthesizing nanoparticles. Journal of Materials Research and Technology. 2023 Nov 1;27:1739–63.

19. Reinmann R, Akram M. Temporal investigation of a fast spark discharge in chemically inert gases. J Phys D: Appl Phys. 1997 Apr;30(7):1125.

20. Pfeiffer T, Kedia P, Messing M, Valvo M, Schmidt-Ott A. Precursor-Less Coating of Nanoparticles in the Gas Phase. Materials. 2015 Mar 11;8(3):1027–42.

21. Tabrizi NS, Ullmann M, Vons VA, Lafont U, Schmidt-Ott A. Generation of nanoparticles by spark discharge. J Nanopart Res. 2009 Feb;11(2):315–32.

22. Hallberg RT, Ludvigsson L, Preger C, Meuller BO, Dick KA, Messing ME. Hydrogen-assisted spark discharge generated metal nanoparticles to prevent oxide formation. Aerosol Science and Technology. 2018 Mar 4;52(3):347–58.

23. Petallidou KC, Ternero P, Messing ME, Schmidt-Ott A, Biskos G. Tuning atomic-scale mixing of nanoparticles produced by atmospheric-pressure spark ablation. Nanoscale Adv. 2023;5(24):6880–6.

24. Snellman M, Eom N, Messing ME, Deppert K. A thermal evaporator for aerosol core-shell nanoparticle synthesis. Journal of Aerosol Science. 2024 Jan;175:106276.

25. Weber AP, Seipenbusch M, Thanner C, Kasper G. Aerosol Catalysis on Nickel Nanoparticles.

26. Jung W, Jung YH, Pikhitsa PV, Feng J, Yang Y, Kim M, et al. Three-dimensional nanoprinting via charged aerosol jets. Nature. 2021 Apr;592(7852):54–9.

27. Kangasluoma J, Cai R, Jiang J, Deng C, Stolzenburg D, Ahonen LR, et al. Overview of measurements and current instrumentation for 1–10 nm aerosol particle number size distributions. Journal of Aerosol Science. 2020 Oct;148:105584.

28. Hinds WC. Aerosol Technology: Properties, Behavior, and Measurement of Airborne Particles. Subsequent edition. New York: Wiley-Interscience; 1999. 483 p.

29. Chen DR, Pui DYH, Hummes D, Fissan H, Quant FR, Sem GJ. Design and evaluation of a nanometer aerosol differential mobility analyzer (Nano-DMA). Journal of Aerosol Science. 1998 Jun 1;29(5):497–509.

30. Fuchs NA. On the stationary charge distribution on aerosol particles in a bipolar ionic atmosphere. Geofisica Pura e Applicata. 1963;56(1):185–93.

31. Brilke S, Resch J, Leiminger M, Steiner G, Tauber C, Wlasits PJ, et al. Precision characterization of three ultrafine condensation particle counters using singly charged salt clusters in the 1–4 nm size range generated by a bipolar electrospray source. Aerosol Science and Technology. 2020 Apr 2;54(4):396–409.

32. Fissan H, Ristig S, Kaminski H, Asbach C, Epple M. Comparison of different characterization methods for nanoparticle dispersions before and after aerosolization. Anal Methods. 2014 Jul 15;6(18):7324.

33. Karlsson LS, Deppert K, Malm JO. Size Determination of Au Aerosol Nanoparticles by Off-Line TEM/STEM Observations. J Nanopart Res. 2006 Dec 1;8(6):971–80.

34. Harra J, Juuti P, Haapanen J, Sorvali M, Roumeli E, Honkanen M, et al. Coating of Silica and Titania Aerosol Nanoparticles by Silver Vapor Condensation. Aerosol Science and Technology. 2015 Sep 2;49(9):767–76.

35. Gao J, Liu Q, Gu F, Liu B, Zhong Z, Su F. Recent advances in methanation catalysts for the production of synthetic natural gas. RSC Adv. 2015 Feb 26;5(29):22759–76.

36. Hejral U, Vlad A, Nolte P, Stierle A. In Situ Oxidation Study of Pt Nanoparticles on MgO(001). J Phys Chem C. 2013 Oct 3;117(39):19955–66.

37. Lopez N. On the origin of the catalytic activity of gold nanoparticles for low-temperature CO oxidation. Journal of Catalysis. 2004 Apr 1;223(1):232–5.

38. Molina LM, Hammer B. Some recent theoretical advances in the understanding of the catalytic activity of Au. Applied Catalysis A: General. 2005 Sep;291(1–2):21–31.

39. Backman U, Tapper U, Jokiniemi JK. An aerosol method to synthesize supported metal catalyst nanoparticles. Synthetic Metals. 2004 Apr 13;142(1):169–76.

40. Lähde A, Raula J, Kauppinen EI. Combined synthesis and in situ coating of nanoparticles in the gas phase. J Nanopart Res. 2008 Dec 1;10(1):121–30.

41. von der Weiden SL, Drewnick F, Borrmann S. Particle Loss Calculator – a new software tool for the assessment of the performance of aerosol inlet systems. Atmospheric Measurement Techniques. 2009 Sep 3;2(2):479–94.

42. Zhang H, Sharma G, Dhawan S, Dhanraj D, Li Z, Biswas P. Comparison of discrete, discrete-sectional, modal and moment models for aerosol dynamics simulations. Aerosol Science and Technology. 2020 Jul 2;54(7):739–60.

43. Lehtinen KEJ, Zachariah MR. Energy accumulation in nanoparticle collision and coalescence processes. Journal of Aerosol Science. 2002 Feb;33(2):357–68.

44. Buffat Ph, Borel JP. Size effect on the melting temperature of gold particles. Phys Rev A. 1976 Jun 1;13(6):2287–98.

45. Castro T, Reifenberger R, Choi E, Andres RP. Size-dependent melting temperature of individual nanometer-sized metallic clusters. Phys Rev B. 1990 Nov 1;42(13):8548–56.

46. Arcidiacono S, Bieri NR, Poulikakos D, Grigoropoulos CP. On the coalescence of gold nanoparticles. International Journal of Multiphase Flow. 2004 Jul;30(7–8):979–94.

47. Kofman R, Cheyssac P, Aouaj A, Lereah Y, Deutscher G, Ben-David T, et al. Surface melting enhanced by curvature effects. Surface Science. 1994 Feb;303(1–2):231–46.

48. Barr TL. An ESCA study of the termination of the passivation of elemental metals. J Phys Chem. 1978 Aug;82(16):1801–10.

49. Payne BP, Biesinger MC, McIntyre NS. The study of polycrystalline nickel metal oxidation by water vapour. Journal of Electron Spectroscopy and Related Phenomena. 2009 Dec 1;175(1):55–65.

50. Gao F, Gu Z. Melting Temperature of Metallic NanoparticlesMetal nanoparticlessynthetic methods. In: Aliofkhazraei M, editor. Handbook of Nanoparticles [Internet]. Cham: Springer International Publishing; 2015 [cited 2024 Jun 13]. p. 1–25. Available from: https://doi.org/10.1007/978-3-319-13188-7_6-1

51. Weber AP, Friedlander SK. In situ determination of the activation energy for restructuring of nanometer aerosol agglomerates. Journal of Aerosol Science. 1997 Mar;28(2):179–92.

52. Schlexer P, Andersen AB, Sebok B, Chorkendorff I, Schiøtz J, Hansen TW. Size-Dependence of the Melting Temperature of Individual Au Nanoparticles. Particle & Particle Systems Characterization. 2019;36(3):1800480.

53. Wang G, Xu YS, Qian P, Su YJ. The effects of size and shape on the structural and thermal stability of platinum nanoparticles. Computational Materials Science. 2019 Nov;169:109090.

54. Wu R, Zhao X, Liu Y. Atomic insights of Cu nanoparticles melting and sintering behavior in Cu Cu direct bonding. Materials & Design. 2021 Jan;197:109240.

55. Van Teijlingen A, Davis SA, Hall SR. Size-dependent melting point depression of nickel nanoparticles. Nanoscale Adv. 2020;2(6):2347–51.

56. Eggersdorfer ML, Pratsinis SE. The Structure of Agglomerates Consisting of Polydisperse Particles. Aerosol Science and Technology. 2012 Mar;46(3):347–53.

57. Olszok V, Bierwirth M, Weber AP. Interaction of Reactive Gases with Platinum Aerosol Particles at Room Temperature: Effects on Morphology and Surface Properties. Nanomaterials. 2021 Aug 31;11(9):2266.

58. Meuller BO, Messing ME, Engberg DLJ, Jansson AM, Johansson LIM, Norlén SM, et al. Review of Spark Discharge Generators for Production of Nanoparticle Aerosols. Aerosol Science and Technology. 2012 Nov;46(11):1256–70.

59. Tritt TM. Thermal Conductivity: Theory, Properties, and Applications. Springer Science & Business Media; 2005. 306 p.

60. Moskal A, Payatakes AC. Estimation of the diffusion coefficient of aerosol particle aggregates using Brownian simulation in the continuum regime. Journal of Aerosol Science. 2006 Sep;37(9):1081–101.

61. Wang Y, Liu F, He C, Bi L, Cheng T, Wang Z, et al. Fractal Dimensions and Mixing Structures of Soot Particles during Atmospheric Processing. Environ Sci Technol Lett. 2017 Nov 14;4(11):487–93.

62. Huhtamäki T, Tian X, Korhonen JT, Ras RHA. Surface-wetting characterization using contact-angle measurements. Nat Protoc. 2018 Jul;13(7):1521–38.

63. Labat F, Baranek P, Adamo C. Structural and Electronic Properties of Selected Rutile and Anatase TiO2 Surfaces: An ab Initio Investigation. J Chem Theory Comput. 2008 Feb 1;4(2):341–52.

64. Kinloch AJ. Adhesion and Adhesives [Internet]. Dordrecht: Springer Netherlands; 1987 [cited 2024 May 13]. Available from: http://link.springer.com/10.1007/978-94-015-7764-9

65. Tyson WR, Miller WA. Surface free energies of solid metals: Estimation from liquid surface tension measurements. Surface Science. 1977 Jan;62(1):267–76.